



Synthesis of copper-silver doped hydroxyapatite via ultrasonic coupled sol-gel techniques: structural and antibacterial studies

S. Kamonwannasit¹ · C. M. Futralan² · P. Khemthong³ · T. Butburee³ · A. Karaphun⁴ · P. Phatai⁵ 

Received: 12 May 2020 / Accepted: 25 August 2020
© Springer Science+Business Media, LLC, part of Springer Nature 2020

Abstract

Fabrication of hydroxyapatite (HA) via doping with metal ions to enhance its antibacterial properties has attracted much interest. The present study aims to synthesize copper-silver doped hydroxyapatite particles (Cu-Ag doped HA) with an improved antibacterial activity through a sol-gel technique coupled with ultrasonic irradiation. The doping materials consist of Cu^{2+} and Ag^+ ions with precursor molar ratios of 0.0, 0.25, 0.50, 0.75 and 1.0. The physicochemical properties of $\text{Ca}_{9,0}\text{Cu}_{1,0-x}\text{Ag}_x(\text{PO}_4)_6(\text{OH})_2$ samples were investigated using X-ray diffraction, Fourier-transform infrared spectroscopy (FT-IR), and transmission electron microscopy coupled with energy dispersive X-ray analysis (TEM-EDS). Characterization studies revealed that Cu^{2+} and Ag^+ ions were incorporated into a hexagonal framework of HA. The main functional groups were identified as hydroxyl (OH^-) and phosphate (PO_4^{3-}) moieties. Their morphologies were rod-shaped with various diameters and particle size distributions, depending on the molar ratio of Cu^{2+} to Ag^+ . Antibacterial activity was evaluated using an agar well diffusion method against *Staphylococcus epidermis*, *S. aureus*, *Bacillus subtilis*, *B. cereus*, and *Pseudomonas aeruginosa*. It was found that Cu-Ag doped HA is an effective antibacterial agent. $\text{Ca}_{9,0}\text{Cu}_{0,5}\text{Ag}_{0,5}(\text{PO}_4)_6(\text{OH})_2$ showed the best antibacterial performance against all bacterial strains with inhibition zones ranging from 13 to 17 mm, indicating its suitability as an antibacterial material in biomedical applications.

Supplementary information The online version of this article (<https://doi.org/10.1007/s10971-020-05407-8>) contains supplementary material, which is available to authorized users.

✉ P. Phatai
piaw.ph@udru.ac.th

¹ Faculty of Agricultural Technology, Burapha University, Sakaeo 27160, Thailand

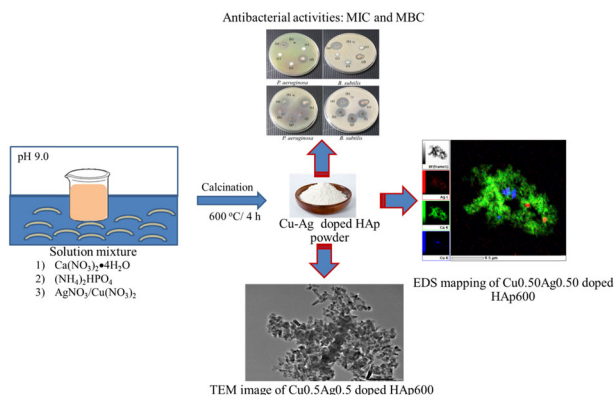
² Department of Environmental Science, Ateneo de Manila University, 1108 Quezon City, Philippines

³ National Nanotechnology Center (NANOTEC), National Science and Technology Development Agency (NSTDA), Pathum Thani 12120, Thailand

⁴ Department of Physics, Faculty of Science, Khon Kaen University, Khon Kaen 40002, Thailand

⁵ Department of Chemistry, Faculty of Science, Udon Thani Rajabhat University, Udon Thani 41000, Thailand

Graphical Abstract



Keywords Antibacterial activity · Copper · Hydroxyapatite · Silver · Sol-gel technique

Highlights

1. Ultrasonic treatment combined with a sol-gel technique synthesized well dispersed, rod-shaped Cu-Ag doped HA.
2. $\text{Ca}_{9.0}\text{Cu}_{0.5}\text{Ag}_{0.5}(\text{PO}_4)_6(\text{OH})_2$ has excellent antibacterial activity against Gram-positive and Gram-negative bacteria.
3. Cu-Ag doped HA nanoparticle is an effective antibacterial material in biomedical applications.

1 Introduction

Hydroxyapatite [$\text{Ca}_{10}(\text{PO}_4)_6(\text{OH})_2$, HA] is an essential constituent of vertebrae, teeth, and bones [1]. Extensive applications of HA are possible due to its bioactivity, thermodynamic stability, excellent osteoconductivity, superior biocompatibility, and nontoxicity [2–5]. HA can be successfully prepared via various chemical methods such as emulsions [6], sol-gel [7], wet chemical precipitation [8], microwave [9], and hydrothermal processes [10]. Among these, sol-gel route is considered an attractive preparative method in comparison to other processes since it can be performed at a low crystallization temperature, provide fewer defects, and improved structural integrity [11–13]. Moreover, the sol-gel method is one of the most frequently applied synthesis techniques due to its flexibility, capacity for ionic substitution in the material, excellent chemical homogeneity, low-cost, and ease of operation [14–16]. However, the synthesis of HA via sol-gel technique requires a long reaction time to complete the reaction between the calcium (Ca) and phosphorous (P) precursors [17, 18]. In addition, the sol-gel technique often results in agglomerated HA particles that would lead to poor antibacterial properties [19, 20]. An ultrasonic coupled sol-gel technique is considered a facile and effective method to adjust the structures and properties of nanomaterials owing to its cavitation effect [19, 21–23]. Cavitation can enhance heterogeneous reactions between the liquid and solid phases during HA synthesis, resulting in particles with uniform shapes and

sizes, less agglomeration, and high crystallinity [23–25]. Other advantages of using ultrasonic methods include cost-effectiveness, smaller quantities of chemicals utilized, and higher phase purity [22, 23, 26, 27].

Several commercial applications of HA include dentistry, maxillofacial and orthopedic surgery, drug delivery, coatings on metallic prostheses, bone cement, and fillers. However, pure HA cannot be utilized in load-supporting applications because of its low mechanical stability and brittleness [28]. In addition, bacterial infections of HA ceramic during or after implantation have become a significant problem that can lead to prolonged pain and implant failure [29]. HA material is comprised mainly of calcium and phosphate, which do not provide any resistance to bacterial infection [30]. Recent studies focused on improving the antibacterial activity of implant materials via incorporation of cations to overcome the shortcomings of pure HA.

Atomic substitution or doping of HA with certain ions is an attractive approach to improve its antibacterial properties and impart mechanical strength to bioceramic materials [28]. Substitution of Cu^{2+} , Ag^+ , Zn^{2+} cations into the HA matrix has been reported [5, 13, 29–32]. Several studies on HA modified by Ag^+ have demonstrated broad-spectrum antibacterial efficacy [33–36]. However, a high concentration of Ag^+ in HA is known to cause argyria and increased cytotoxicity [37]. Incorporation of a second metal ion such as Cu^{2+} is necessary to mitigate these negative impacts and retain the optimal antibacterial effect of Ag [38]. Cu^{2+} is known to promote metabolism via production of cross-linked

collagen and improved enzymatic activity [39]. Furthermore, use of Cu^{2+} would yield non-toxic biomaterials with excellent antimicrobial efficacy and improved mechanical integrity [32, 40–43]. Our extensive literature review revealed that substitution of Ag^+ and Cu^{2+} into HA via an ultrasonic coupled sol-gel route has not yet been reported.

Thus, in the present work, synthesis of Cu-Ag doped HA nanoparticles by ultrasonic coupled sol-gel techniques was investigated. The effect of the molar ratios between Cu^{2+} and Ag^+ ions in $\text{Ca}_{9.0}\text{Cu}_{1.0-x}\text{Ag}_x(\text{PO}_4)_6(\text{OH})_2$ was studied. The antibacterial activities against five bacterial strains, including *Staphylococcus epidermis*, *S. aureus*, *Bacillus subtilis*, *B. cereus*, and *Pseudomonas aeruginosa* were evaluated. The minimum inhibitory concentration (MIC) and minimum bactericidal concentration (MBC) were also determined using an agar well diffusion method.

2 Materials and methods

2.1 Materials and microorganisms

All chemical reagents were of analytical grade and utilized without further purification. Calcium nitrate tetrahydrate ($\text{Ca}(\text{NO}_3)_2 \cdot 4\text{H}_2\text{O}$, 99.9 wt.%, QREC), diammonium hydrogen phosphate ($(\text{NH}_4)_2\text{HPO}_4$, 98.0 wt.%, UNIVAR), silver nitrate (AgNO_3 , 99.9 wt.%, POCh), copper nitrate ($\text{Cu}(\text{NO}_3)_2$, 98.0 wt.%, UNIVAR) and an ammonia solution (NH_3 , 30 wt.%, Carlo Erba) were acquired. The Gram-negative bacterium, *P. aeruginosa* (TISTR 781), and Gram-positive bacteria, *S. aureus* (TISTR 1466), *S. epidermis* (TISTR 518), *B. subtilis* (TISTR 008), and *B. cereus* (TISTR 687) were obtained from the Thailand Institute of Scientific and Technological Research (TISTR) and were carried using nutrient agar slants.

2.2 Synthesis of Cu-Ag doped HA samples

HA nanoparticles with the chemical formula, $\text{Ca}_{9.0}\text{Cu}_{1.0-x}\text{Ag}_x(\text{PO}_4)_6(\text{OH})_2$, denoted as Cu-Ag doped HA, were synthesized via an ultrasonic technique coupled with a sol-gel method. Prior to synthesis, each solution of $\text{Ca}(\text{NO}_3)_2 \cdot 4\text{H}_2\text{O}$, $(\text{NH}_4)_2\text{HPO}_4$, AgNO_3 , and $\text{Cu}(\text{NO}_3)_2$ was individually prepared by dissolving the precursors in DI water. Then, an $(\text{NH}_4)_2\text{HPO}_4$ solution was added drop-wise into the $\text{Ca}(\text{NO}_3)_2 \cdot 4\text{H}_2\text{O}$ solution in an ultrasonic bath with a frequency of 37 kHz over a period of 0.5 h. Next, solutions of AgNO_3 and $\text{Cu}(\text{NO}_3)_2$ with the desired molar ratio (0.0, 0.25, 0.50, 0.75 and 1.0) were added drop-wise into the mixture during ultrasonication for 0.5 h. After this, the pH of the mixture was adjusted to 9.0 ± 0.1 using 1.0 M NH_4OH . Each of the mixtures was stirred continuously on a hotplate at 100 °C until dry. Finally, the dried samples were calcined at 600 °C

in a muffle furnace (SNOL 30/1100 LSF21) for 4 h with a heating rate of 3 °C/min. The final products are referred to as $\text{Ca}_{9.0}\text{Cu}_{1.0-x}\text{Ag}_x(\text{PO}_4)_6(\text{OH})_2$ where x denotes the molar ratio of the Cu and Ag precursors. They were labeled as Cu1.0 doped HA600, Cu0.75Ag0.25 doped HA600, Cu0.50Ag0.50 doped HA600, Cu0.25Ag0.75 doped HA600 and Ag1.0 doped /HA600, respectively. The as-synthesized samples were labeled as HA100 and Cu-Ag doped HA100.

2.3 Characterization techniques

The crystallinity and phase identification of the HA samples were evaluated using X-ray diffraction (XRD) (D8 Advance Series 2, Bruker, Germany) employing an accelerating voltage of 40 kV with Cu $K\alpha$ radiation ($\lambda = 1.54184 \text{ \AA}$) and 35 mA. The functional groups of HA samples were determined using Fourier-transform infrared spectroscopy (FT-IR) spectroscopy (Spectrum Two, Perkin Elmer, USA) over the spectral range of 4000–500 cm^{-1} with a 4 cm^{-1} resolution. The morphology, particle size distribution, and elemental mapping of HA samples were analyzed using transmission electron microscopy (TEM) (JEOL JEM-2100, Japan) operated at 200 kV. The samples were dispersed in a methanol medium and then deposited onto carbon film coated Ni TEM grids. The sample showing the highest antibacterial activity was characterized using energy dispersive X-ray (EDS) analysis.

2.4 Antibacterial activity

2.4.1 Agar well diffusion method

An agar well diffusion technique was employed to evaluate the antibacterial activities of the HA samples [44]. First, bacterial strains were cultured in a Mueller-Hinton broth (MHB) at 37 °C for 18 h with a 0.5 McFarland turbidity standard. Then, each of the bacterial cultures (100 μL , 10^8 CFU/mL) was spread onto separate Mueller-Hinton agar plates. Using a sterile cork borer, 5 mm diameter wells were cut into the agar medium and 50 μL aliquots of HA were subsequently added to each well. After that, the inoculated plates were incubated at 37 °C for 24 h before employing 30 μg tetracycline as a positive control. Finally, the resulting inhibition zones (mm) were determined by assessing the width of the clear zones around the wells. All assays were performed in triplicate using aseptic technique.

2.4.2 Determination of minimum inhibitory concentration (MIC) and minimum bactericidal concentration (MBC)

MIC refers to the lowest concentration of antibacterial agents where no visible bacterial growth is observed after

24 h incubation at 37 °C. MBC is defined as the lowest concentration of agent where there is no occurrence of sub-culture growth [45]. Based on the methodology of Kamonwannasit et al. [45], the MIC against bacteria (10^7 CFU/mL) was determined with various concentrations of Cu-Ag doped HA (10, 15, and 20 mg/mL) in MHB where incubation of the inoculated tubes was carried out at 37 °C for 24 h. The MBC was determined where 100 μ L from each tube was sub-cultured onto fresh Mueller-Hinton agar plates and incubated at 37 °C for 24 h with no visible bacterial growth. All experimental runs were performed in triplicate.

3 Results and discussion

3.1 XRD analysis

Figure 1 displays the phase composition and lattice parameters of Cu-Ag doped HA100 samples and HA100. In all HA samples, broad, dispersed peaks within 31.0° to 34.0° are observed, which suggests the presence of amorphous phases. This indicates that the precursors ($\text{Ca}(\text{NO}_3)_2 \cdot 4\text{H}_2\text{O}$, $(\text{NH}_4)_2\text{HPO}_4$, AgNO_3 , and $\text{Cu}(\text{NO}_3)_2$) did not react completely during oven-drying at 110 °C. The spectra showed the triclinic structure of dicalcium phosphate anhydrous (CaHPO_4) (*P-1* space group) with the corresponding 2 θ peaks at 26.0° (0 0 2), 29.1° (2 1 0), 31.8° (2 1 1), 32.3° (1 1 2), 33.0° (3 0 0) and 40.1° (3 1 0) (JCPDS No. 09-0432). Moreover, a single phase HA was not completely formed in the as-synthesized samples, which is in agreement with our previous work [17].

The XRD spectra of the calcined samples are illustrated in Fig. 2. It was found that all calcined samples exhibited the typical hexagonal crystal structure of HA (*P6₃/m* space group) with corresponding 2 θ peaks at 25.92° (0 0 2), 32.18° (2 1 0), 33.0° (2 1 1), 34.1° (1 1 2), 39.9° (3 0 0), 46.7° (2 2 2), 48.17° (2 1 3) and 53.2° (0 0 4) (JCPDS No. 09-0432). A pure HA phase was obtained only in HA600 and Cu1.0 doped HA600 samples. In Cu-Ag doped HA samples, secondary phases including beta-tricalcium phosphate (β -TCP, $\text{Ca}_3(\text{PO}_4)_2$) and calcium oxide (CaO) were identified. The presence of β -TCP can be correlated to the main peaks at 2 θ with values of 21.8° (0 2 4), 25.9° (1 0 10), 28.1° (2 1 4), 31.8° (0 2 10), 34.1° (2 2 0) and 35.5° (2 1 10) (JCPDS No. 09-0169) while CaO is attributed to the peak at 38.1° (2 0 0). This could be due to the decomposition of HA caused by chemical impurities or elevated temperatures [46–48]. Normally, a material made of both HA and β -TCP is called biphasic calcium phosphate (BCP). It can promote bone remodeling and new bone formation since partial dissolution of BCP releases calcium and phosphate ions in the local environment [49].

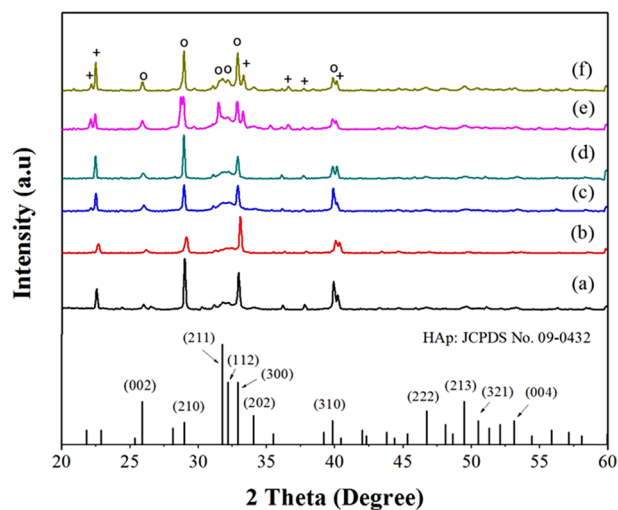


Fig. 1 XRD spectra of (a) HA100, (b) Cu1.0 doped HA100, (c) Cu0.75Ag0.25 doped HA100, (d) Cu0.50Ag0.50 doped HA100, (e) Cu0.25Ag0.75 doped HA100 and (f) Ag1.0 doped HA100. [o HA, + CaHPO_4]

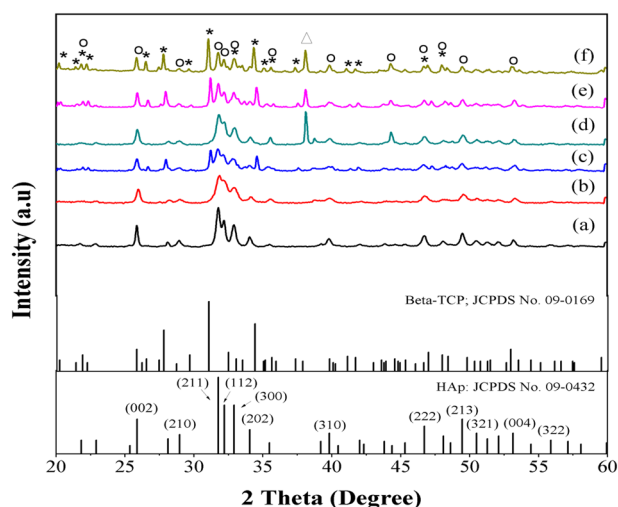


Fig. 2 XRD spectra of (a) HA600, (b) Cu1.0 doped HA600, (c) Cu0.75Ag0.25 doped HA600, (d) Cu0.50Ag0.50 doped HA600, (e) Cu0.25Ag0.75 doped HA600 and (f) Ag1.0 doped HA600. [o HA, * β -TCP, Δ CaO]

The characteristic peaks of Ag_2O (JCPDS No. 01-1041), $\text{Ag}_3(\text{PO}_4)$ (JCPDS No. 01-1058), and CuO (JCPDS No. 01-1117) were not observed. This result confirms the homogeneous distribution of copper and silver ions in the crystal structure of HA, even at high concentrations of dopants. Moreover, the molar fraction of Cu^{2+} and Ag^+ ions was very small compared to HA in the samples. This could be the reason for the absence of Ag_2O , $\text{Ag}_3(\text{PO}_4)$, and CuO peaks. Similar results have been reported in previous studies [31, 50, 51].

Table 1 Lattice parameter, unit cell volume and crystallite size of Cu-Ag doped HA600 samples obtained from XRD analysis

Samples	Lattice parameters (nm)		Crystallite size (nm)
	<i>a</i>	<i>c</i>	
HA600	0.9421 ± 0.0012	0.6889 ± 0.0004	27.10
Cu1.0 doped HA600	0.9411 ± 0.0005	0.6931 ± 0.0096	17.25
Cu0.75Ag0.25 doped HA600	0.9424 ± 0.0006	0.6872 ± 0.0008	24.45
Cu0.50Ag0.50 doped HA600	0.9430 ± 0.0014	0.6951 ± 0.0100	38.00
Cu0.25Ag0.75 doped HA600	0.9429 ± 0.0006	0.6877 ± 0.0001	37.05
Ag1.0 doped HA600	0.9428 ± 0.0004	0.6889 ± 0.0010	37.75

For a general hexagonal crystal system, the lattice parameters (*a* and *c*) can be calculated using Eq. (1)[52]:

$$\frac{1}{d_{hkl}} = \left[\frac{4(h^2 + k^2 + hk)}{3a^2} + \left(\frac{l^2}{c^2} \right) \right]^{1/2}, \quad (1)$$

where *h*, *k*, and *l* are the Miller indices of the crystal plane, while *a* and *c* are the lattice parameters. The average *a* value of the HA samples was calculated using the (210) and (310) plane indices, while the average *c* value was computed using the (002) and (004) plane indices. As illustrated in Table 1, the “*a*” and “*c*” values of the Cu-Ag doped HA600 samples are close to those of stoichiometric HA (JCPDS No. 09-0432; *a* = 0.9418 nm and *c* = 0.6884 nm). There was no significant difference between the lattice parameters of samples. This could be due to the small amount of Cu²⁺ and Ag⁺ ions in the crystal lattice of HA.

The average crystallite size *D* (nm) of the sample powders was computed using the Scherrer equation:

$$D = \frac{k\lambda}{\beta \cos\theta}, \quad (2)$$

where λ is the wavelength of Cu K α radiation ($\lambda = 0.15418$ nm), β is the full width at half maximum (FWHM) of a given reflection (radians), θ is the corresponding Bragg diffraction angle (°) and *k* is the broadening constant that varies with the crystal type [53, 54]. For quantitative determinations, the peaks at (0 0 2), (2 0 2), and (2 1 3) reflections were used to calculate the crystallite sizes of HA powders. The peaks are well resolved and displayed no interference. In Table 1, it can be observed that the average crystallite size of HA600 (27.10 nm) was larger than that of Cu1.0 doped HA600 (17.25 nm) and smaller than that of Ag1.0 doped HA600 (37.75 nm). In the case of Cu-Ag doped HA, the crystallite size increased with the Ag⁺ content. These results were attributed to differences in ionic radii.

3.2 FT-IR analysis

FT-IR spectra of the as-synthesized and calcined samples are displayed in Figs. 3 and 4, respectively. The main

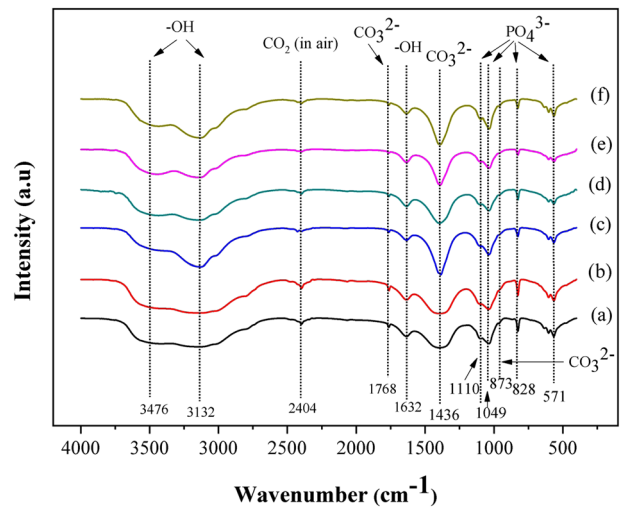


Fig. 3 FT-IR spectra of (a) HA100, (b) Cu1.0 doped HA100, (c) Cu0.75Ag0.25 doped HA100, (d) Cu0.50Ag0.50 doped HA100, (e) Cu0.25Ag0.75 doped HA100 and (f) Ag1.0 doped HA100

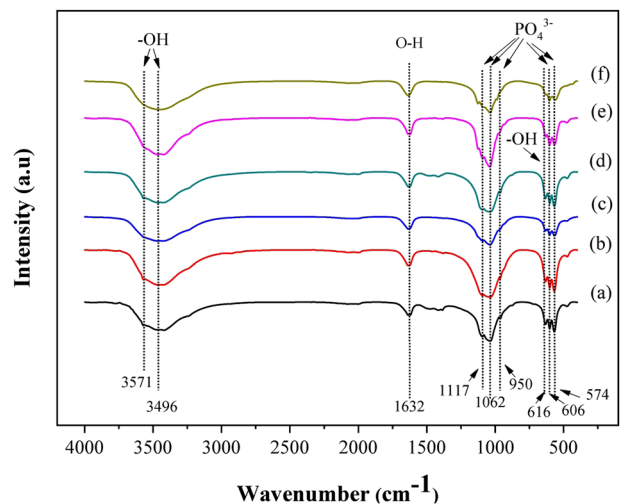


Fig. 4 FT-IR spectra of (a) HA600 (b) Cu1.0 doped HA600 (c) Cu0.75Ag0.25 doped HA600 (d) Cu0.50Ag0.50 doped HA600 (e) Cu0.25Ag0.75 doped HA600 and (f) Ag1.0 doped HA600

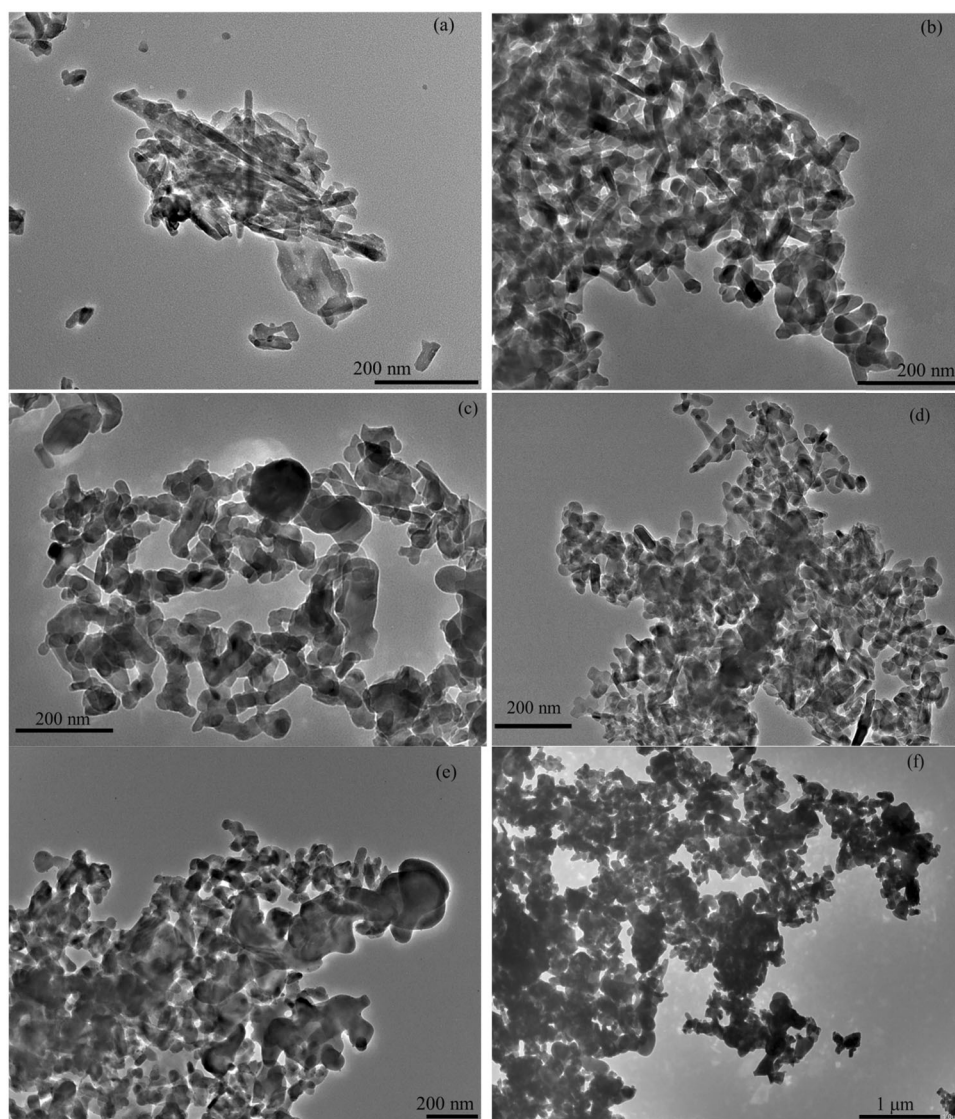
vibrational modes of the PO₄³⁻ and -OH groups correspond to the HA structure. In Fig. 3, as-synthesized samples are

characterized by broad peaks extending from ~ 3000 to 3600 cm^{-1} and 1632 cm^{-1} that correspond to the stretching and bending modes of hydroxyl groups from physisorbed water molecules, respectively. The sharp bands at $1049\text{--}1110\text{ cm}^{-1}$ refer to the ν_2 bending mode (O–P–O bond) of tetragonal PO_4^{3-} while the peaks at 571 and 618 cm^{-1} indicate the ν_4 bending mode of the O–P–O linkage in the PO_4^{3-} group [55]. The presence of carbonate (CO_3^{2-}) is confirmed by bands at 1768 , 1651 , 873 , and $\sim 1300\text{--}1500\text{ cm}^{-1}$ due to the stretching modes of its C=O and C–O groups. This revealed that a certain level of carbonate substitution occurred, which is attributed to the dissolution of atmospheric CO_2 into the aqueous solution during synthesis [56, 57] or the residual nitrates and ammonia (NO_3^- and NH_4^+) derived from the precursors used in the synthesis of powders. The band at 2404 cm^{-1} is due to atmospheric CO_2 contamination during analysis.

However, some differences between the spectra of the as-synthesized and calcined samples were observed. In the calcined samples, the peak at 3000 to 3600 cm^{-1} that results from absorbed $-\text{OH}$ is observed to be narrower in comparison to the as-synthesized HA. Two new peaks were observed at 3571 and 616 cm^{-1} that are ascribed to the ν_s stretching vibration band of O–H and ν_L vibrational mode of OH (O–H bond) in the HA lattice, respectively. These peaks indicate the crystalline nature of HA [42]. The small peak at 950 cm^{-1} corresponds to the symmetric ν_1 stretching mode of the phosphate group, which confirms formation of the characteristic HA structure. In calcined samples, the peaks of carbonate were not detected. This result is supported by the XRD analysis where the degree of crystallinity increased with the calcination temperature.

Based on the XRD and FT-IR results, it is observed that the HA600 and Cu–Ag doped HA600 samples exhibited the

Fig. 5 TEM images of as-synthesized HA samples calcined at $600\text{ }^\circ\text{C}$ for 4 h: (a) HA600, (b) Cu1.0 doped HA600, (c) Cu0.75Ag0.25 doped HA600, (d) Cu0.50Ag0.50 doped HA600, (e) Cu0.25Ag0.75 doped HA600 and (f) Ag1.0 doped HA600



phases of crystalline HA and β -TCP. Based on previous studies, the presence of HA and β -TCP implies an improvement in antibacterial activity [21, 58].

3.3 TEM analysis

Figure 5 shows TEM images of pure HA and Cu-Ag doped HA calcined at 600 °C. Overall, the HA particles in the samples tend to aggregate because sample particles may not be well dispersed in a methanol medium. The morphology of HA600 consists of small, rod-shaped particles that are 20.45 ± 4.91 nm in diameter (Fig. 5a). The morphologies of Cu1.0 doped HA600 (Fig. 5b) and Cu0.75Ag0.25 doped HA600 (Fig. 5c) show agglomerations of small, elongated, and rod-shaped HA nanoparticles with diameters of 23.58 ± 5.45 and 34.82 ± 13.72 nm, respectively. In Fig. 5d, well dispersed rod-shaped HA nanoparticles of Cu0.50Ag0.50 doped HA600 with 19.59 ± 6.48 nm diameters were observed. The Cu0.25Ag0.75 doped HA sample (Fig. 5e) shows aggregated HA nanoparticles 57.51 ± 17.04 nm in diameter. Moreover, several dark spots with diameters of less than 5 nm were detected that could be comprised of Ag^+ and Cu^{2+} species. The nanoparticles were densely distributed on the HA surface, which indicates agglomeration of HA. Meanwhile, the presence of Ag^+ and Cu^{2+} indicates the replacement of Ca^{2+} by Ag^+ and Cu^{2+} . The Ag1.0 doped HA sample (Fig. 5f) showed densely aggregated HA that is 54.94 ± 20.15 nm in diameter. These results confirmed that the presence of Ag^+ and/or Cu^{2+} could regulate nano-powder morphology. This supports the XRD results, indicating that Ag^+ and Cu^{2+} were incorporated into the HA structure. The nano-sized HA and the distribution of Ag^+ and Cu^{2+} nanoparticles could have a great impact on improving the mechanical and antibacterial properties of Cu-Ag doped HA materials.

3.4 Antibacterial activities

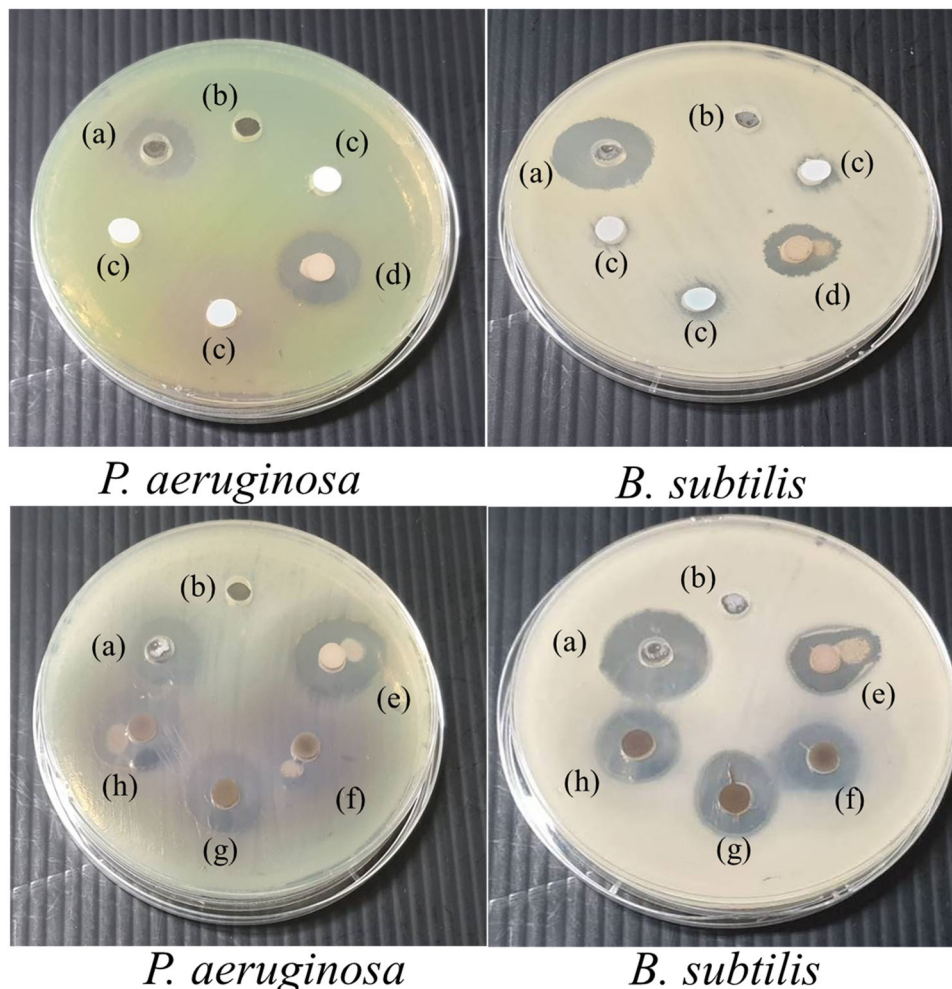
The antibacterial activities of HA600 and Cu-Ag doped HA600 samples at a concentration of 10 mg/mL were evaluated against five bacterial strains. The inhibitory effect of the samples against bacterial growth was compared based upon their zones of inhibition. Bacterial strains with more susceptibility to antimicrobial agents display larger inhibition zones. The width of the zones of inhibition around wells with Cu-Ag doped HA nanoparticles against the test strains after 24 h of incubation is shown in Table 2 and Fig. 6. The positive tetracycline control was effective against all bacterial strains at 30 μg where its inhibition zones range from 16 to 37 mm. Of the as-synthesized HA powders, HA600 demonstrated no inhibition of bacterial growth against any strain. For the Cu1.0 doped HA600 sample, only *S. epidermidis* and *B. subtilis*

Table 2 Diameter of inhibition zones of calcined samples against five different bacterial strains (ND = no detection)

Types of bacteria	Inhibition diameter (mm) (10 mg/mL)	Tetracycline (30 μg)
HA600		
<i>S. epidermidis</i>	ND	–
<i>S. aureus</i>	ND	–
<i>B. subtilis</i>	ND	–
<i>B. cereus</i>	ND	–
<i>P. aeruginosa</i>	ND	–
Cu1.0 doped HA600		
<i>S. epidermidis</i>	14.05 ± 0.95	–
<i>S. aureus</i>	ND	–
<i>B. subtilis</i>	12.55 ± 0.95	–
<i>B. cereus</i>	ND	–
<i>P. aeruginosa</i>	ND	–
Cu0.75Ag0.25 doped HA600		
<i>S. epidermidis</i>	15.61 ± 1.39	–
<i>S. aureus</i>	13.39 ± 1.61	–
<i>B. subtilis</i>	14.88 ± 0.41	–
<i>B. cereus</i>	15.48 ± 0.89	–
<i>P. aeruginosa</i>	18.25 ± 0.83	–
Cu0.5Ag0.5 doped HA600		
<i>S. epidermidis</i>	13.68 ± 0.43	–
<i>S. aureus</i>	14.55 ± 1.93	–
<i>B. subtilis</i>	15.38 ± 1.77	–
<i>B. cereus</i>	15.34 ± 0.17	–
<i>P. aeruginosa</i>	17.88 ± 0.00	–
Cu0.25Ag0.75 doped HA600		
<i>S. epidermidis</i>	14.26 ± 0.07	–
<i>S. aureus</i>	12.89 ± 1.13	–
<i>B. subtilis</i>	16.12 ± 4.10	–
<i>B. cereus</i>	14.56 ± 0.55	–
<i>P. aeruginosa</i>	18.80 ± 1.85	–
Ag1.0 doped HA600		
<i>S. epidermidis</i>	19.63 ± 3.84	–
<i>S. aureus</i>	14.86 ± 1.63	–
<i>B. subtilis</i>	12.67 ± 1.41	–
<i>B. cereus</i>	21.13 ± 3.77	–
<i>P. aeruginosa</i>	15.61 ± 0.35	–
Tetracycline		
<i>S. epidermidis</i>	–	36.83 ± 0.62
<i>S. aureus</i>	–	29.05 ± 0.86
<i>B. subtilis</i>	–	19.11 ± 1.39
<i>B. cereus</i>	–	23.90 ± 1.39
<i>P. aeruginosa</i>	–	16.12 ± 0.74

exhibited inhibition zones that were determined to be 14.05 and 12.55 mm, respectively. The antibacterial activity of Ag1.0 doped HA600 nanoparticles was effective against

Fig. 6 Photographs of the antibacterial activity of calcined samples against gram negative bacteria *P. aeruginosa* and gram positive bacteria *B. subtilis* at a dose of 10 mg/mL: (a) Positive control, (b) negative control, (c) HA600, (d) Ag1.0 doped HA600, (e) Cu0.25Ag0.75 doped HA600, (f) Cu1.0 doped HA600, (g) Cu0.50Ag0.50 doped HA600 and (h) Cu0.75Ag0.25 doped HA600



both Gram-negative and Gram-positive bacteria with inhibition zones ranging from 12 to 21 mm. Dual doped Cu-Ag doped HA nanoparticles showed similar antibacterial activity to that of the single Ag doped HA where all bacterial strains were inhibited. In comparison to the study of Jadalannagari et al. [59], the antibacterial activity against *S. aureus* of Cu0.50Ag0.50 doped HA600 containing 5% Ag5%Cu codoped HA was higher than that of 5%Ag doped HA. The largest inhibition zones (17 to 19 mm) were observed for *P. aeruginosa*. This Gram-negative bacterium was more sensitive to Ag-Cu doped HA600 nanoparticles than Gram-positive strains (*S. epidermidis*, *S. aureus*, *B. subtilis*, and *B. cereus*). The membranes of Gram-negative bacteria have negative electrostatic charges that attract and facilitate diffusion of Ag-Cu doped HA nanoparticles. Results obtained in the present work are similar to the study of Jadalannagari et al. [59]. In addition, gram-negative bacteria have cell walls that are relatively thinner than those of Gram-positive species. In general, soluble Ag⁺ and Cu²⁺ ions are typically found in ionic form. When aliquot Cu-Ag doped HA samples are loaded into marked

agar wells, Ag⁺ and Cu²⁺ ions diffuse out of the wells and penetrate into the bacterial cells. This in turn kills or inhibits the surrounding bacteria and prevents bacterial growth. The release of Ag⁺ and/or Cu²⁺ ions is an important factor that would enhance the antibacterial activity of a medical device [60]. Gram-positive bacteria are more resistant to Ag⁺ ions because their cell wall consists of a thick peptidoglycan layer composed of teichoic acids, which limit their uptake of silver nanoparticles. However, the specific response of each bacterium depends upon their metabolic characteristics.

MIC is noted as the lowest concentration of an antimicrobial substance that will inhibit the visible growth of a microorganism after 24 h of incubation. It is an effective indicator of inhibitory efficacy. To determine the MIC values of all samples, the inhibitory efficacy of 10, 15, and 20 mg/mL NPs was tested against *P. aeruginosa* since this strain is the most sensitive to the Cu-Ag doped HA samples. In Table 3, the MIC value of 20 mg/mL was attained for Cu0.75Ag0.25 doped HA600 sample while a lower MIC value of 15 mg/mL was obtained for Cu0.50Ag0.50 doped

Table 3 MIC and MBC of calcined samples against *P. aeruginosa*

Samples	Concentration (mg/mL)	
	MIC	MBC
Cu1.0 doped HA600	–	–
Cu0.75Ag0.25 doped HA600	20	>20
Cu0.50Ag0.50 doped HA600	15	>20
Cu0.25Ag0.75 doped HA600	15	>20
Ag1.0 doped HA600	15	>20

HA600, Cu0.25Ag0.75 doped HA600 and Ag1.0 doped HA600. Meanwhile, the MBC values were determined to be > 20 mg/mL for *P. aeruginosa*, indicating the bactericidal activity of all samples. It is known that high concentrations of Ag⁺ ions cause cytotoxicity to cells [60, 61], so it is important to determine a minimum Ag⁺ concentration that would demonstrate antibacterial activity. The present study showed that the optimal Cu:Ag molar ratio of 0.5:0.5 (Cu0.50Ag0.50 doped HA600) is sufficient for bactericidal activity. This condition is well below the limit of

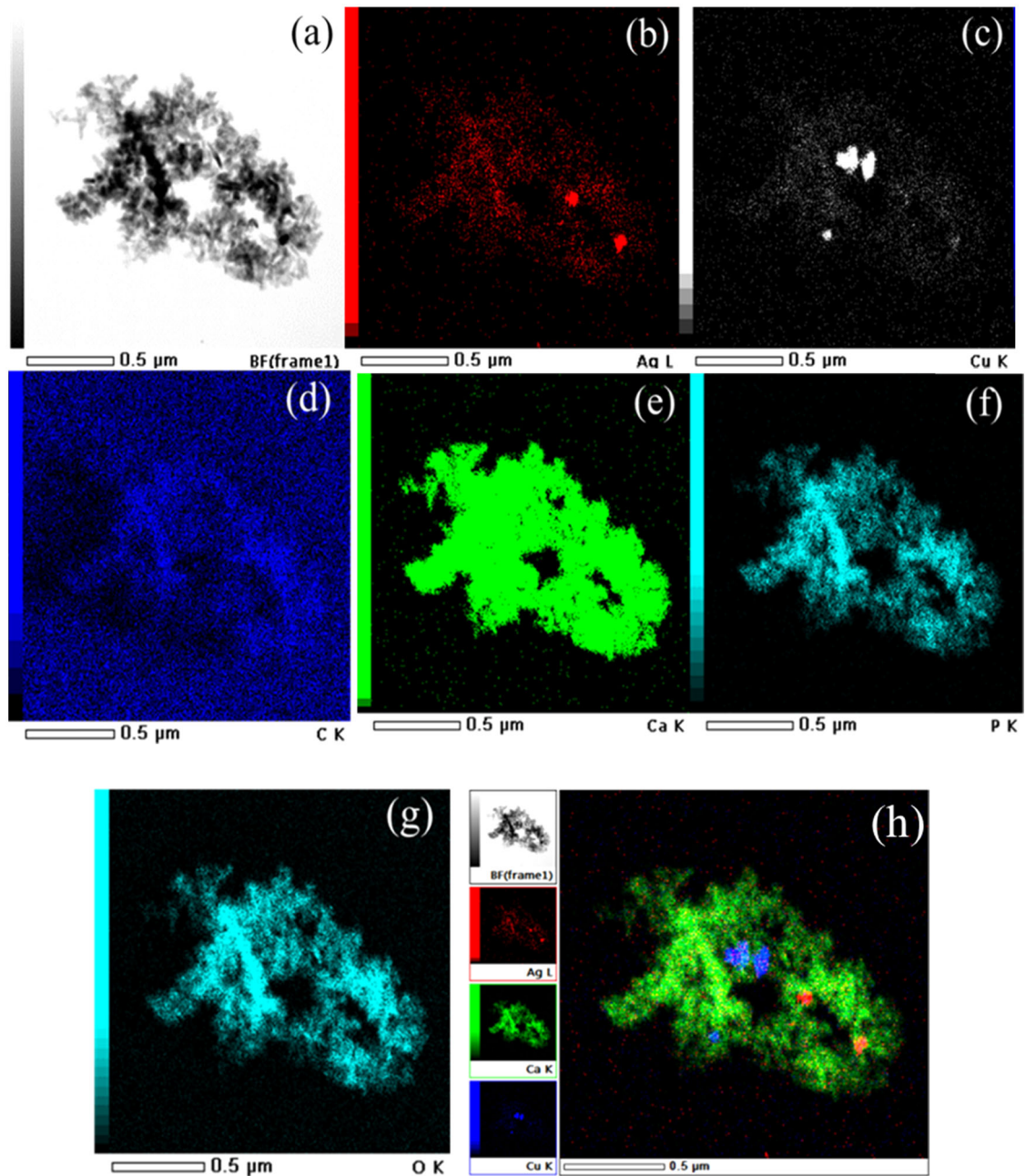


Fig. 7 EDS mapping shows elemental distribution of Cu0.50Ag0.50 doped HA600 structure: (a) secondary electron image; (b–g) the element sensitive maps of Ag, Cu, C, Ca, P and O in the structure, respectively and (h) combination of Cu, Ag and Ca maps

cytotoxicity [60, 61]. Moreover, a lower Ag^+ content implies reduced cost of fabrication of HA nanoparticles.

Based on the results of antibacterial activity tests, $\text{Cu}_0.50\text{Ag}_0.50$ doped HA600 showed the best performance. So, it was further characterized using EDS to map the elements detected in the material (Fig. 7). It can be seen that Ag nanoparticles were uniformly distributed in the HA matrix. Alternatively, Cu^{2+} was found in more aggregated clusters. Based on the information in Fig. S1 (Supplementary information), the principle constituents of $\text{Cu}_0.50\text{Ag}_0.50$ doped HA600 were Ca, P, Cu, Ag, and O. The presence of C and Ni can be attributed to the carbon film on nickel grid during analysis. Moreover, the $(\text{Ca} + \text{Ag} + \text{Cu})/\text{P}$ atomic ratio of $\text{Cu}_0.50\text{Ag}_0.50$ doped HA600 was 1.74, which is higher than that of the stoichiometric HA ratio (1.67). This could be attributed to the substitution of PO_4^{3-} by CO_3^{2-} [19, 21]. Moreover, the small diameter and well dispersed rod-like HA nanoparticles of $\text{Cu}_0.50\text{Ag}_0.50$ doped HA600 imply that the nanoparticles might possess high surface area. A high surface area indicates greater release rates of dissolved Ag^+ and Cu^{2+} ions that would correspond to enhanced antibacterial activity. This result is in agreement with the study of Buckley et al. [62] that reported Ag^+ ions adsorbed onto high surface area HA ($204 \text{ m}^2 \text{ g}^{-1}$) displayed improved antibacterial performance against *S. aureus* and *P. aeruginosa*.

4 Conclusions

Ultrasonic irradiation coupled with a sol-gel technique can produce a highly homogeneous silver-copper doped HA bioceramic with excellent antibacterial properties. XRD results confirmed the formation of mixed crystalline phases of HA, β -TCP, and CaO after calcination at 600°C . However, no phosphate or oxides of silver and copper were detected. Results obtained from FT-IR are in complete agreement with the XRD analysis. Transmission electron microscopy coupled with energy dispersive X-ray analysis confirmed the homogeneous distribution of silver and copper particles in the HA lattice. An agar well diffusion method was employed to study the antibacterial activity against five strains of bacteria. Results show that $\text{Cu}_0.50\text{Ag}_0.50/\text{HA600}$ with a $(\text{Ca} + \text{Ag} + \text{Cu})/\text{P}$ atomic ratio of 1.74 provided excellent antibacterial activity against both Gram-positive and Gram-negative bacteria.

Acknowledgements We would like to acknowledge the Department of Chemistry (Faculty of Science) and the Research and Development Institute of the Udon Thani Rajabhat University (Thailand) for their financial support of this research undertaking. Many thanks to Professor Dr. Jeffrey C. Nash from the Office of Graduate Studies of the

Udon Thani Rajabhat University (Thailand) for his assistance in proofreading this manuscript.

Compliance with ethical standards

Conflict of interest The authors declare that they have no conflict of interest.

Publisher's note Springer Nature remains neutral with regard to jurisdictional claims in published maps and institutional affiliations.

References

1. Tamai N, Myoui A, Tomita T et al. (2002) Novel hydroxyapatite ceramics with an interconnective porous structure exhibit superior osteoconduction in vivo. *J Biomed Mater Res* 59:110–117. <https://doi.org/10.1002/jbm.1222>
2. Hench LL (1998) Bioceramics. *J Am Ceram Soc* 81:1705–1728. <https://doi.org/10.1111/j.1151-2916.1998.tb02540.x>
3. Hayashi K, Mashima T, Uenoyama K (1999) The effect of hydroxyapatite coating on bony ingrowth into grooved titanium implants. *Biomaterials* 20:111–119. [https://doi.org/10.1016/S0142-9612\(98\)00011-8](https://doi.org/10.1016/S0142-9612(98)00011-8)
4. Li T-T, Ling L, Lin M-C et al. (2019) Effects of ultrasonic treatment and current density on the properties of hydroxyapatite coating via electrodeposition and its in vitro biomineralization behavior. *Mater Sci Eng C* 105:110062. <https://doi.org/10.1016/j.msec.2019.110062>
5. Kumar GS, Thamizhavel A, Yokogawa Y et al. (2012) Synthesis, characterization and in vitro studies of zinc and carbonate co-substituted nano-hydroxyapatite for biomedical applications. *Mater Chem Phys* 134:1127–1135. <https://doi.org/10.1016/j.mchemphys.2012.04.005>
6. Wong WY, Mohd Noor A-F (2016) Synthesis and sintering-wet carbonation of nano-sized carbonated hydroxyapatite. *Procedia Chem* 19:98–105. <https://doi.org/10.1016/j.proche.2016.03.121>
7. Ben-Arfa BAE, Miranda Salvado IM, Ferreira JMF, Pullar RC (2017) Novel route for rapid sol-gel synthesis of hydroxyapatite, avoiding ageing and using fast drying with a 50-fold to 200-fold reduction in process time. *Mater Sci Eng C* 70:796–804. <https://doi.org/10.1016/j.msec.2016.09.054>
8. Yelten-Yilmaz A, Yilmaz S (2018) Wet chemical precipitation synthesis of hydroxyapatite (HA) powders. *Ceram Int* 44:9703–9710. <https://doi.org/10.1016/j.ceramint.2018.02.201>
9. Sabu U, Logesh G, Rashad M, Joy A, Balasubramanian M (2019) Microwave assisted synthesis of biomorphic hydroxyapatite. *Ceram Int* 45:6718–6722. <https://doi.org/10.1016/j.ceramint.2018.12.161>
10. Nosrati H, Mamoory RS, Svend Le DQ et al. (2020) Gas injection approach for synthesis of hydroxyapatite nanorods via hydrothermal method. *Mater Charact* 159:110071. <https://doi.org/10.1016/j.matchar.2019.110071>
11. Fihri A, Len C, Varma RS, Solhy A (2017) Hydroxyapatite: A review of syntheses, structure and applications in heterogeneous catalysis. *Coord Chem Rev* 347:48–76. <https://doi.org/10.1016/j.ccr.2017.06.009>
12. Balani K, Chen Y, Harimkar SP et al. (2007) Tribological behavior of plasma-sprayed carbon nanotube-reinforced hydroxyapatite coating in physiological solution. *Acta Biomater* 3:944–951. <https://doi.org/10.1016/j.actbio.2007.06.001>
13. Ramires PA, Romito A, Cosentino F, Milella E (2001) The influence of titania/hydroxyapatite composite coatings on in vitro osteoblasts behaviour. *Biomaterials* 22:1467–1474. [https://doi.org/10.1016/S0142-9612\(00\)00269-6](https://doi.org/10.1016/S0142-9612(00)00269-6)

14. Neira IS, Kolen'ko YV, Lebedev OI et al. (2009) An effective morphology control of hydroxyapatite crystals via hydrothermal synthesis. *Cryst Growth Des* 9:466–474. <https://doi.org/10.1021/cg800738a>
15. Kim H-W, Kong Y-M, Bae C-J et al. (2004) Sol-gel derived fluor-hydroxyapatite biocoatings on zirconia substrate. *Biomaterials* 25:2919–2926. <https://doi.org/10.1016/j.biomaterials.2003.09.074>
16. Kaur S, Bala N, Khosla C (2013) Preparation and deposition of hydroxyapatite on biomaterials by sol-gel technique-a review. *Chitkara Chemistry Review* 1:59–69. <https://doi.org/10.15415/ccr.2013.12011>
17. Liu DM, Troczynski T, Tseng WJ (2002) Aging effect on the phase evolution of water-based sol-gel hydroxyapatite. *Biomaterials* 23:1227–1236. [https://doi.org/10.1016/s0142-9612\(01\)00242-3](https://doi.org/10.1016/s0142-9612(01)00242-3)
18. Yan Q, Qiu M, Chen X, Fan Y (2019) Ultrasound assisted synthesis of size-controlled aqueous colloids for the fabrication of nanoporous zirconia membrane. *Front Chem* 7:1–10. <https://doi.org/10.3389/fchem.2019.00337>
19. Phatai P, Futralan CM, Utara S et al. (2018) Structural characterization of cerium-doped hydroxyapatite nanoparticles synthesized by an ultrasonic-assisted sol-gel technique. *Results Phys* 10:956–963. <https://doi.org/10.1016/j.rinp.2018.08.012>
20. Lamkhao S, Phaya M, Jansakun C et al. (2019) Synthesis of hydroxyapatite with antibacterial Properties Using a microwave-assisted combustion method. *Sci Rep* 9:1–9. <https://doi.org/10.1038/s41598-019-40488-8>
21. Phatai P, Futralan CM, Kamonwannasit S, Khemthong P (2019) Structural characterization and antibacterial activity of hydroxyapatite synthesized via sol-gel method using glutinous rice as a template. *J Sol-Gel Sci Technol* 89:764–775. <https://doi.org/10.1007/s10971-018-4910-9>
22. Utara S, Klinkaewnarong J (2015) Sonochemical synthesis of nano-hydroxyapatite using natural rubber latex as a templating agent. *Ceram Int* 41:14860–14867. <https://doi.org/10.1016/j.ceramint.2015.08.018>
23. Utara S, Klinkaewnarong J (2015) Effect of sonication time on the characteristics of nanophase hydroxyapatite crystals synthesized by the sol-gel technique. *Micro Nano Lett* 10:1–4. <https://doi.org/10.1049/mnl.2014.031620>
24. Kim W, Saito F (2001) Sonochemical synthesis of hydroxyapatite from H₃PO₄ solution with Ca(OH)₂. *Ultrason Sonochem* 8:85–88. [https://doi.org/10.1016/s1350-4177\(00\)00034-1](https://doi.org/10.1016/s1350-4177(00)00034-1)
25. Rouhani P, Taghavinia N, Rouhani S (2010) Rapid growth of hydroxyapatite nanoparticles using ultrasonic irradiation. *Ultrason Sonochem* 17:853–856. <https://doi.org/10.1016/j.ultsonch.2010.01.010>
26. Sadat-Shojai M, Khorasani M-T, Dinpanah-Khoshdargi E, Jamshidi A (2013) Synthesis methods for nanosized hydroxyapatite with diverse structures. *Acta Biomater* 9:7591–7621. <https://doi.org/10.1016/j.actbio.2013.04.012>
27. Gopi D, Govindaraju KM, Victor CAP et al. (2008) Spectroscopic investigations of nanohydroxyapatite powders synthesized by conventional and ultrasonic coupled sol-gel routes. *Spectrochim Acta A Mol Biomol Spectrosc* 70:1243–1245. <https://doi.org/10.1016/j.saa.2008.02.015>
28. Fakhrazadeh A, Ebrahimi-Kahrizsangi R, Nasiri-Tabrizi B, Jeffrey Basirun W (2017) Effect of dopant loading on the structural features of silver-doped hydroxyapatite obtained by mechanochemical method. *Ceram Int* 43:12588–12598. <https://doi.org/10.1016/j.ceramint.2017.06.136>
29. Iqbal N, Abdul Kadir MR, Nik Malek NAN et al. (2013) Characterization and antibacterial properties of stable silver substituted hydroxyapatite nanoparticles synthesized through surfactant assisted microwave process. *Mater Res Bull* 48:3172–3177. <https://doi.org/10.1016/j.materresbull.2013.04.068>
30. Hedrick TL, Adams JD, Sawyer RG (2006) Implant-associated infections: an overview. *J Long Term Eff Med* 16:83–99. <https://doi.org/10.1615/jlongtermeffmedimplants.v16.i1.90>
31. Shanmugam S, Gopal B (2014) Copper substituted hydroxyapatite and fluorapatite: Synthesis, characterization and antimicrobial properties. *Ceram Int* 40:15655–15662. <https://doi.org/10.1016/j.ceramint.2014.07.086>
32. Batebi K, Abbasi Khazaei B, Afshar A (2018) Characterization of sol-gel derived silver/fluor-hydroxyapatite composite coatings on titanium substrate. *Surf Coat Technol* 352:522–528. <https://doi.org/10.1016/j.surfcoat.2018.08.021>
33. Rameshbabu N, Sampath Kumar TS, Prabhakar TG et al. (2007) Antibacterial nanosized silver substituted hydroxyapatite: synthesis and characterization. *J Biomed Mater Res A* 80:581–591. <https://doi.org/10.1002/jbm.a.30958>
34. Gristina AG (1987) Biomaterial-centered infection: microbial adhesion versus tissue integration. *Science* 237:1588–1595. <https://doi.org/10.1126/science.3629258>
35. Kazachenko AS, Legler AV, Per'yanova OV, Vstavskaya YuA (2000) Synthesis and antimicrobial activity of silver complexes with histidine and tryptophan. *Pharm Chem J* 34:257–258. <https://doi.org/10.1007/BF02524634>
36. Rai M, Yadav A, Gade A (2009) Silver nanoparticles as a new generation of antimicrobials. *Biotechnol Adv* 27:76–83. <https://doi.org/10.1016/j.biotechadv.2008.09.002>
37. Hidalgo E, Domínguez C (1998) Study of cytotoxicity mechanisms of silver nitrate in human dermal fibroblasts. *Toxicol Lett* 98:169–179. [https://doi.org/10.1016/s0378-4274\(98\)00114-3](https://doi.org/10.1016/s0378-4274(98)00114-3)
38. Gopi D, Shinyjoy E, Kavitha L (2014) Synthesis and spectral characterization of silver/magnesium co-substituted hydroxyapatite for biomedical applications. *Spectrochim Acta A Mol Biomol Spectrosc* 127:286–291. <https://doi.org/10.1016/j.saa.2014.02.057>
39. Ghosh R, Swart O, Westgate S et al. (2019) Antibacterial copper-hydroxyapatite composite coatings via electrochemical synthesis. *Langmuir* 35:5957–5966. <https://doi.org/10.1021/acs.langmuir.9b00919>
40. Unabia RB, Bonebeau S, Candidato RT, Pawłowski L (2018) Preliminary study on copper-doped hydroxyapatite coatings obtained using solution precursor plasma spray process. *Surf Coat Technol* 353:370–377. <https://doi.org/10.1016/j.surfcoat.2018.09.008>
41. Kim TN, Feng QL, Kim JO et al. (1998) Antimicrobial effects of metal ions (Ag⁺, Cu²⁺, Zn²⁺) in hydroxyapatite. *J Mater Sci Mater Med* 9:129–134. <https://doi.org/10.1023/A:1008811501734>
42. Turkoz M, Atilla AO, Evis Z (2013) Silver and fluoride doped hydroxyapatites: Investigation by microstructure, mechanical and antibacterial properties. *Ceram Int* 39:8925–8931. <https://doi.org/10.1016/j.ceramint.2013.04.088>
43. Landi E, Sprio S, Sandri M et al. (2008) Development of Sr and CO₃ co-substituted hydroxyapatites for biomedical applications. *Acta Biomater* 4:656–663. <https://doi.org/10.1016/j.actbio.2007.10.010>
44. Sen A, Batra AA (2012) Evaluation of antimicrobial activity of different solvent extracts of medicinal plant: *Melia Azedarach* L. *Int J Curr Pharm Res* 4:67–73
45. Kamonwannasit S, Nantapong N, Kumkrai P et al. (2013) Antibacterial activity of *Aquilaria crassna* leaf extract against *Staphylococcus epidermidis* by disruption of cell wall. *Ann Clin Microbiol Antimicrob* 12:20. <https://doi.org/10.1186/1476-0711-12-20>
46. Guo X, Yan H, Zhao S et al. (2013) Effect of calcining temperature on particle size of hydroxyapatite synthesized by solid-state reaction at room temperature. *Adv Powder Technol* 24:1034–1038. <https://doi.org/10.1016/j.apt.2013.03.002>

47. Sompech S, Dasri T, Thaomola S (2016) Preparation and characterization of amorphous silica and calcium oxide from agricultural wastes. *Orient J Chem* 32:1923–1928. <https://doi.org/10.13005/ojc/320418>
48. Hayakawa S, Hajima Y, Qiao S et al. (2008) Characterization of calcium carbonate polymorphs with Ca K edge X-ray absorption fine structure spectroscopy. *Anal Sci* 24:835–837. <https://doi.org/10.2116/analsci.24.835>
49. Daculsi G, Laboux O, Malard O, Weiss P (2003) Current state of the art of biphasic calcium phosphate bioceramics. *J Mater Sci Mater Med* 14:195–200. <https://doi.org/10.1023/A:1022842404495>
50. Labanni A, Zulhadjri, Handayani D, Ohya Y, Arief S (2020) Size controlled synthesis of well-distributed nano-silver on hydroxyapatite using alkanolamine compounds. *Ceram Int* 46:5850–5855. <https://doi.org/10.1016/j.ceramint.2019.11.035>
51. Grigoraviciute-Puroniene I, Stankeviciute Z, Ishikawa K, Kar-eiva A (2020) Formation of calcium hydroxyapatite with high concentration of homogeneously distributed silver. *Micropor Mesopor Mat* 293:xxx. <https://doi.org/10.1016/j.micromeso.2019.109806>
52. Zhang P, Lu H, Zhou Y, et al (2015) Mesoporous MnCeOx solid solutions for low temperature and selective oxidation of hydrocarbons. *Nat Commun* 6. 10.1038/ncomms9446
53. Chen C-W, Oakes CS, Byrappa K et al. (2004) Synthesis, characterization, and dispersion properties of hydroxyapatite prepared by mechanochemical–hydrothermal methods. *J Mater Chem* 14:2425–2432. <https://doi.org/10.1039/B315095J>
54. Monshi A, Foroughi MR, Monshi MR (2012) Modified Scherrer equation to estimate more accurately nano-crystallite size using XRD. *World J Nano Sci Eng* 2:154–160. <https://doi.org/10.4236/wjnse.2012.23020>
55. Türk S, Altınsoy İ, ÇelebiEfe G et al. (2017) Microwave–assisted biomimetic synthesis of hydroxyapatite using different sources of calcium. *Mater Sci Eng C* 76:528–535. <https://doi.org/10.1016/j.msec.2017.03.116>
56. Cheng ZH, Yasukawa A, Kandori K, Ishikawa T (1998) FTIR Study of Adsorption of CO₂ on Nonstoichiometric Calcium Hydroxyapatite. *Langmuir* 14:6681–6686. <https://doi.org/10.1021/la980339n>
57. Waheed S, Sultan M, Jamil T, Hussain T (2015) Comparative analysis of hydroxyapatite synthesized by sol-gel, ultrasonication and microwave assisted technique. *Mater Today Proc* 2:5477–5484. <https://doi.org/10.1016/j.matpr.2015.11.073>
58. Gopi D, Bhuvaneshwari N, Indira J et al. (2013) A novel green template assisted synthesis of hydroxyapatite nanorods and their spectral characterization. *Spectrochim Acta A Mol Biomol Spectrosc* 107:196–202. <https://doi.org/10.1016/j.saa.2013.01.052>
59. Jadalannagari S, Deshmukh K, Ramanan SR, Kowshik M (2014) Antimicrobial activity of hemocompatible silver doped hydroxyapatite nanoparticles synthesized by modified sol–gel technique. *Appl Nanosci* 4:133–141. <https://doi.org/10.1007/s13204-013-0197-x>
60. Nath S, Kalmodia S, Basu B (2010) Densification, phase stability and in vitro biocompatibility property of hydroxyapatite-10 wt% silver composites. *J Mater Sci Mater Med* 21:1273–1287. <https://doi.org/10.1007/s10856-009-3939-2>
61. Rajendran A, Barik RC, Natarajan D et al. (2014) Synthesis, phase stability of hydroxyapatite–silver composite with antimicrobial activity and cytocompatibility. *Ceram Int* 40:10831–10838. <https://doi.org/10.1016/j.ceramint.2014.03.075>
62. Buckley JJ, Lee AF, Olivi L, Wilson K (2010) Hydroxyapatite supported antibacterial Ag₃PO₄ nanoparticles. *J Mater Chem* 20:8056–8063. <https://doi.org/10.1039/c0jm01500h>